# Breaking the diffraction limit by saturation in stimulated-Raman-scattering microscopy: A theoretical study

Li Gong and Haifeng Wang*
*Department of Physics, National University of Singapore, Singapore, 117542*
(Received 30 January 2014; published 15 July 2014)

We present a theoretical investigation on the saturation of stimulated Raman scattering (SRS) and propose an application of it to break the diffraction limit in SRS microscopy. In our proposed scheme, a donut-shaped Stokes beam is used to saturate SRS at the rim of a focused Gaussian pump beam; thus the addition of another Gaussian Stokes beam can only induce additional stimulated Raman loss to the pump beam in a small area inside the donut-shaped beam. Resembling stimulated-emission-depletion microscopy, this method can significantly improve the lateral imaging resolution. Compared with the diffraction-limited resolution, theoretical simulations show that it may be possible to double the spatial resolution with a few TW/cm$^2$ of laser intensity. Such super-resolution could greatly enhance the advantage of SRS microscopy for potential applications.

DOI: 10.1103/PhysRevA.90.013818 PACS number(s): 42.65.Dr, 42.25.Fx, 87.64.M−, 87.64.kp

## I. INTRODUCTION

Super-resolution optical microscopy has become a hot research topic in recent years. The resolution of far-field optical imaging is usually limited by the size of diffraction patterns, close to the wavelength of illumination. However, with proper manipulation of the illumination field or sample properties, it is possible to extract spatial features much smaller than the diffraction limit, leading to super-resolution. Stimulated-emission-depletion (STED) microscopy [1], stochastic-optical-reconstruction microscopy (STORM) [2], and structured-illumination microscopy (SIM) [3] are the most successful examples in this area. Nevertheless, these methods were mostly used to enhance the resolution of fluorescence microscopy. There are also super-resolution methods based on nonlinear mechanisms such as the saturation of electronic absorption [4] and photothermal effects [5]. SIM can be combined with nonlinear mechanisms to provide super-resolution as well [6,7].

Another growing area in optical microscopy in recent years is coherent-Raman-imaging methods such as coherent anti-Stokes Raman-scattering (CARS) microscopy [8,9] and stimulated-Raman-scattering (SRS) microscopy [10,11]. Conventionally, both these methods illuminate the sample with two laser beams, called the pump and Stokes beams. The pump beam has a higher frequency $\omega_p$, and the Stokes beam has a lower frequency $\omega_S$. When the frequency difference $\omega_p-\omega_S$ is equal to the frequency of a molecular vibrational mode (denoted as $\Omega$), a transition from the ground state to the vibrational state will occur due to resonance. This resonance stimulates the generation of a new field at a blue-shifted frequency $2\omega_p-\omega_S$, which is the CARS output. At the same time, the resonant transitions also cause the pump beam to experience a loss in the medium and the Stokes beam to experience a gain. These are called stimulated Raman loss (SRL) and stimulated Raman gain (SRG), respectively, which are the two aspects of SRS. SRS microscopy may detect either SRL or SRG as the signal. Both CARS and SRS microscopy have the unique advantage of providing chemical contrast without the need for labeling, which is very attractive to many biomedical applications. On the other hand, CARS microscopy may suffer from a nonresonant background generated by electronic transitions [8], while SRS microscopy is a newer method that is intrinsically free of nonresonant background [10].

As CARS and SRS are nonlinear processes, they require high excitation intensity and the laser beams must be tightly focused into the sample by a high numerical aperture (NA) objective. Like other nonlinear microscopy methods, the spatial resolution is determined by the size of the excitation volume, which is again determined by the diffraction-limited focal spot size. Usually, the lateral resolution in these methods can reach $\lambda/3$–$\lambda/2$. But in the last few years, several schemes have been proposed to achieve super-resolution in far-field CARS microscopy [12–19]. The mechanisms involved can be summarized in four types. In the first type, a control beam is adopted to generate side bands of CARS signal due to Rabi oscillation. When the control beam is more intense at the center of the focal spot than at the rim, a larger Rabi frequency shift is generated at the center, thus sub-diffraction-limited resolution can be achieved by distinguishing the frequency shifted CARS signal [12,13]. A resolution of 65 nm is possible with this method [12]. The second and third types of method both aim to diminish the CARS signal at the rim of the diffraction-limited focal spot with a donut-shaped control beam, but the second type utilizes incoherent coupling between the ground state and the vibrational state [14–16], and the third type utilizes additional probe-beam-induced photon depletion [17]. Resembling STED microscopy, the resolution of these two methods is better with a stronger control beam, allowing theoretically unlimited resolution. But, practically, the resolution enhancement is limited by noise and photodamage [16]. Also, the first and the second types of method only work for resonant CARS signals but not for nonresonant CARS signals. The fourth type of method applies structured illumination or focal volume engineering to CARS microscopy for super-resolution [18–20]. These methods have little dependence on sample properties or the nature of the emitted signal, but the resolution enhancement is limited by a factor of 2–3.

Here we present a scheme, saturated SRS microscopy, to achieve super-resolution. In our scheme, a donut-shaped

*phywh@nus.edu.sg

 

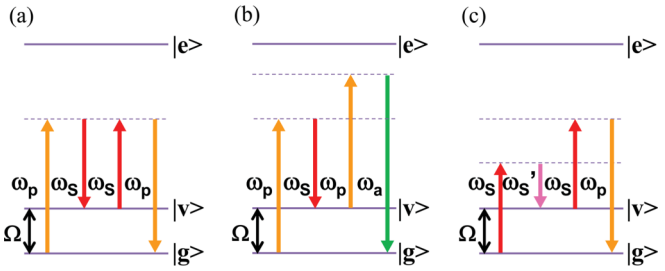


FIG. 1. (Color online) The energy diagram of various nonlinear Raman-scattering processes (following Ref. [21]). The molecule has a ground state $|g\rangle$, a vibrational state $|v\rangle$, and an electronic state $|e\rangle$. There are two incident beams at frequencies $\omega_p$ and $\omega_S$, where $\omega_p - \omega_S$ equals the vibrational frequency $\Omega$. (a) Stimulated Raman scattering (SRS). (b) Coherent anti-Stokes Raman scattering (CARS). (c) Coherent Stokes Raman scattering (CSRS). All figures represent four-wave-mixing processes with no implication on time ordering.

Stokes beam is introduced to make the SRL signal saturated at the rim of the focal spot, thus the addition of another Gaussian Stokes beam can only induce additional SRL signal in a small area inside the donut-shaped beam, leading to super-resolution. The mechanism of resolution enhancement is similar to STED microscopy and some super-resolution CARS techniques mentioned above [14–17]. However, super-resolution SRS microscopy has its own advantages. Compared with fluorescence and other nonvibrational techniques, SRS provides chemical contrast without the need for labeling; compared with CARS, SRS is inherently free of nonresonant background which may obscure the image contrast. Therefore, super-resolution SRS microscopy could be very attractive if realized. In the following, we will introduce the theoretical analysis on the saturation condition of SRS, and then an experimental design with simulation results. In principle, super-resolution can be achieved with either SRL or SRG signal, but since most SRS microscopes detect SRL, we will focus on SRL in this paper.

## II. THEORETICAL FRAMEWORK TO CALCULATE SRL SIGNAL

A typical Raman process occurs in a three-level system, which contains a ground state $|g\rangle$, a vibrational state $|v\rangle$, and an electronic state $|e\rangle$ (Fig. 1). The reason we need the electronic state is that the electronic dipole moments $\mu_{ge} = \langle g|e\mathbf{r}|e\rangle$ and $\mu_{ve} = \langle v|e\mathbf{r}|e\rangle$ being nonzero are necessary conditions for Raman scattering [21]. Normally, this implies that the ground state and the vibrational state have the same parity, so that $\mu_{gv} = \langle g|e\mathbf{r}|v\rangle$ vanishes [21]. The status of the three-level system is described by the density matrix $\rho_{ij}$, where $i, j = g, v, e$. When two laser beams at frequencies $\omega_p$ and $\omega_S$ illuminate the system, and assuming that $\omega_p - \omega_S$ equals the molecular vibrational frequency $\Omega$, the three kinds of nonlinear Raman processes shown in Fig. 1 may take place resonantly [21].

Figure 1(a) shows that SRS is a four-wave-mixing process. Normally, according to Boltzmann distribution, most of the molecules are on the ground state $|g\rangle$, so that in SRS, there will be a net loss of pump photons (SRL) and a net gain of the same number of Stokes photons (SRG). As a result of energy conservation, the same number of molecules will be excited to the vibrational state $|v\rangle$. However, if the excitation is strong enough to make the molecules equally distributed between $|g\rangle$ and $|v\rangle$, the SRL (or SRG) will be saturated. This property will be studied in detail in this work. Figure 1(b) describes the CARS process, in which an anti-Stokes photon at $\omega_a = 2\omega_p - \omega_S$ and a Stokes photon are created, while two pump photons are annihilated. Fig. 1(c) is the coherent Stokes Raman-scattering (CSRS) process, in which a CSRS photon ($\omega'_S = 2\omega_S - \omega_p$) and a pump photon are created, while two Stokes photons are annihilated.

Now we shall focus on the SRL signal or the loss of pump energy due to the interaction with the Stokes laser. In theory, there are both Raman and non-Raman processes which can contribute to such signal. The Raman processes involved are mainly CARS, CSRS, and SRS. At resonance, the energy exchange caused by CARS and CSRS are expected to be several orders of magnitude smaller than SRS [22], and so they can be ignored in the calculation. The non-Raman processes involved are mainly multiphoton absorption. If these processes are not at resonant condition, their signals should be much lower than that of SRS. This is supported by the fact that SRS microscopy images were essentially background free in the literature. Based on these considerations, we assume that SRS is the dominant pathway of annihilating pump photons.

In the next, we need to find a method to calculate the loss of pump photons. SRS causes the loss of a pump photon by causing a transition from $|g\rangle$ to $|v\rangle$ in a molecule. In theory, there are other mechanisms of $|g\rangle$ to $|v\rangle$ transition including IR absorption and spontaneous Raman scattering. Spontaneous Raman scattering is known to be much weaker than SRS with picosecond excitation, and IR absorption should be negligible since the incident laser frequencies are far from the resonant absorption frequency. Thus approximately we can consider SRS as the only pathway of $|g\rangle$ to $|v\rangle$ transition, and the loss of pump photons is directly proportional to the population of molecules that went from $|g\rangle$ to $|v\rangle$. Furthermore, we assume that all molecules are on the ground state in the beginning. This is because for typical Raman bands in the 400–3400 $\text{cm}^{-1}$ region, the Boltzmann factor at room temperature is very small. Thus after light-matter interaction, the number of annihilated pump photons per unit volume should be equal to the number of molecules at the vibrational state per unit volume, which is $N\rho_{vv}$, where $N$ represents the number density of resonant molecules. The actual value of $N$ does not matter much because it only affects the magnitude of the SRL signal, but has nothing to do with the saturation behavior we will study. $\rho_{vv}$ is the key parameter that dictates the behavior of the SRL signal. In SRS microscopy, the excitation lasers usually have picosecond pulse duration [10] and are tightly focused into the sample by a high NA objective. In that case the spontaneous decay of the vibrational state within each pulse is very small, since the lifetime of a vibrational state is in the nanosecond regime. In the focal volume, $\rho_{vv}$ will have a spatial distribution which is related to the electric field distributions of laser beams. At any point in the focal volume, the local SRL signal, i.e., the absorbed pump energy per unit volume per pulse, can be

expressed as

$$\frac{\delta E_p}{\delta V} = N\rho_{vv}\hbar\omega_p. \tag{1}$$

Now we need to find out how $\rho_{vv}$ is saturated, depending on the pump and Stokes electric field amplitude. Finding this saturation condition is the key to designing super-resolution SRS microscopy.

In order to quantitatively calculate $\rho_{vv}$, the density matrix equation of motion is adopted here to describe light-matter interaction [23]:

$$\frac{\partial \rho_{lm}}{\partial t} = -i\omega_{lm}\rho_{lm} - \frac{i}{\hbar}[H_{\text{int}},\rho]_{lm} + \Gamma_{lm}(\rho), \tag{2}$$

where $l$, $m = g$, $v$, $e$, and $\omega_{lm} = \omega_l - \omega_m$ is the frequency difference between states. $H_{\text{int}}$ is the Hamiltonian of light-matter interaction described by Eq. (3), in which $\mathbf{E}$ is the electric field of light. $\Gamma$ is the decay matrix described by Eq. (4).

$$H_{\text{int}} = \begin{bmatrix} 0 & 0 & \boldsymbol{\mu}_{ge}\cdot\mathbf{E} \\ 0 & 0 & \boldsymbol{\mu}_{ve}\cdot\mathbf{E} \\ \boldsymbol{\mu}_{eg}\cdot\mathbf{E} & \boldsymbol{\mu}_{ev}\cdot\mathbf{E} & 0 \end{bmatrix}, \tag{3}$$

$$\Gamma = \begin{bmatrix} \Gamma_{eg}\rho_{ee} + \Gamma_{vg}\rho_{vv}, \gamma_{gv}\rho_{gv}, & \gamma_{ge}\rho_{ge} \\ \gamma_{vg}\rho_{vg}, -\Gamma_{vg}\rho_{vv} + \Gamma_{ev}\rho_{ee}, & \gamma_{ve}\rho_{ve} \\ \gamma_{eg}\rho_{eg}, & \gamma_{ev}\rho_{ev}, -(\Gamma_{eg} + \Gamma_{ev})\rho_{ee} \end{bmatrix}. \tag{4}$$

If the pump and the Stokes light are linearly polarized in the $x$ direction, the total electric field can be expressed as

$$\mathbf{E}(t) = [A_p\cos(\omega_p t) + A_S\cos(\omega_S t)]\exp\left[-\frac{2\ln 2(t-t_0)^2}{\tau^2}\right]\mathbf{i}, \tag{5}$$

where $\mathbf{i}$ is the unit vector in the $x$ direction, and $A_p$ and $A_S$ are the field amplitude of pump and Stokes beams, respectively. $\tau$ is the intensity full width at half maximum (FWHM) durations of both pump and Stokes pulses which are set to be 2 ps, and both pulses are centered at $t_0 = 2$ ps.

In this study, we use the ring breathing vibrational mode ($v_1$ mode) of benzene ($C_6H_6$) as an example for our calculation. The Raman shift frequency is $\Omega = \omega_{gv} = 1.8720 \times 10^2$ THz or 993 $\text{cm}^{-1}$ [24]. For benzene, there are several electronic absorption peaks from 235 to 260 nm [25]. In our model, we approximate these close electronic levels as a single level and treat the molecule as a three-level system. Since normally the lowest dipole-allowed electronic excited state plays the most significant role in Raman processes, we set the electronic excitation frequency to be $\omega_{ge} = 7.2498 \times 10^3$ THz (260 nm). The frequencies of pump and Stokes light are set to be $\omega_p = 2.5422 \times 10^3$ THz (741.09 nm) and $\omega_S = 2.3550 \times 10^3$ THz (800 nm), respectively. As discussed in Appendix A, $\boldsymbol{\mu}_{ge}$, $\boldsymbol{\mu}_{eg}$, $\boldsymbol{\mu}_{ve}$, and $\boldsymbol{\mu}_{ev}$ have the same direction and the same modulus with $\mu = 0.0330e$ nm, which are derived under the Condon approximation from the Raman-scattering cross section, the excitation wavelength, and the gaps between energy levels. These four vectors are set to be along the $x$ axis, which is parallel to the electric field.

The decay of the excited states is caused by the vacuum fluctuation and the collision among molecules [23], and the decay rate can be experimentally measured by transient absorption. It was found that the relaxation time is on the order of nanoseconds for both electronic [26] and vibrational states [27]. Since a picosecond laser is used here, the exact value of the decay rate ($\sim 1$ $\text{ns}^{-1}$) almost does not affect the calculation of SRS. Thus $\Gamma_{20}$, $\Gamma_{21}$, and $\Gamma_{10}$ are set to be 1 $\text{ns}^{-1}$ [15,16]. On the other hand, the decay of the off-diagonal elements in the density matrix $\rho_{ij}$ is caused by the decoherence between the states $|i\rangle$ and $|j\rangle$, and the decoherent rate can be estimated by the bandwidth of the absorption spectrum [23]. Also, the decoherent rate between a vibrational state and ground state can be measured by time-resolved CARS [28,29]. In this study, the pump and Stokes light is far from the electronic excitation wavelength; thus the population transition from $|g\rangle$ to $|e\rangle$ is not obvious. However, $\omega_p - \omega_S$ just matches the Raman frequency; the population transition from $|g\rangle$ to $|v\rangle$ happens resonantly. In this sense, only the decoherence between $|g\rangle$ and $|v\rangle$ significantly affects the SRS. Hence, we need accurate values for $\gamma_{gv}$ and $\gamma_{vg}$. For the other four off-diagonal elements $\gamma_{eg}$, $\gamma_{ge}$, $\gamma_{ev}$, and $\gamma_{ve}$, they are roughly set to be 1 $\text{ps}^{-1}$, which is of the right order of magnitude [15,16,21]. In this study, $\gamma_{gv}$ and $\gamma_{vg}$ are set to be 2.8 $\text{ps}^{-1}$, which is estimated from the bandwidth of the spontaneous Raman spectrum of benzene $v_1$ mode vibration [30,31]. Generally, the off-diagonal elements $\gamma$ can be expressed as a summation of two parts: The first part represents homogeneous broadening of linewidth which is the same for every molecule, and the second part is the inhomogeneous broadening. The mechanisms of homogeneous broadening include spontaneous decay which is a single molecule property, and the dephasing caused by collisions between a molecule and its surroundings. The mechanisms of inhomogeneous broadening include Doppler broadening and random Stark shifts experienced by atoms in a solid [23]. Normally, the contribution of spontaneous decay is very small, on the order of $10^{-9}$ $\text{ps}^{-1}$ in the infrared region [32]. In gases with pressure $<10^{-3}$ atm, Doppler broadening dominates $\gamma$; which is on the order of $10^{-4}$ $\text{ps}^{-1}$ in the infrared region [32]. In gases with pressure $>10^{-3}$ atm, the dephasing induced by molecular collision starts to dominate $\gamma$ . For gases at 1 atm, $\gamma$ is on the order of $10^{-3}$ $\text{ps}^{-1}$ [32]. In condensed

matter, the dephasing induced by molecular collision becomes even stronger and $\gamma$ can be as large as 10 ps$^{-1}$ [28].

With all the parameters set, Eq. (2) is solved numerically by the Runge-Kutta algorithm of the fourth order from 0 to 4 ps with 0.035-fs step size. After the calculation, $\rho_{vv}$ at 4 ps is recorded. The choice of 4 ps is based on the consideration that at that point, the light-mater interaction is basically finished and the decay of vibrational state is still negligible, and therefore we can use $\rho_{vv}$ to estimate the loss of pump photons within one pulse.

The following three sections will show the results of three series of calculations. In Sec III we will calculate $\rho_{vv}$ at 4 ps for different $A_p$ and $A_S$ values using the above model. From the results we can see the saturation behavior of SRS and the laser intensity required to achieve saturation. In Sec. IV we will present a super-resolution SRS microscope design based on the saturation of SRS and calculate the lateral resolution at different laser intensities based on the distribution of $\rho_{vv}$ in the focal volume. In Sec. V we will calculate how the resolution enhancement depends on various parameters. From these results we will know the generality of the proposed imaging technique.

## III. THE SATURATION OF SRS

Using the method described above, we calculated the population probability of the vibrational state $\rho_{vv}$ as a function of the linearly polarized electric field amplitude $A_p$ and $A_S$. In the results, $A_p$ and $A_S$ are converted into the peak intensity $I_p$ and $I_S$ by $I = nc\varepsilon_0 A^2/2$, where $n$ is the refractive index of the sample, $c$ is the speed of light in vacuum, and $\varepsilon_0$ is the vacuum permittivity. Here $n$ is 1.50 for benzene.

$\rho_{vv}$ at various $I_p$ and $I_S$ values are drawn in Fig. 2(a). From these results, we can derive that $\rho_{vv}$ is a function of the product of the peak intensities of pump and Stokes pulses ($I_p \times I_S$), as one might expect from the SRS process. A selected curve of $\rho_{vv}$ with $I = I_p = I_S$ is shown in Fig. 2(b). It shows that $\rho_{vv}$ increases with $I$ initially, but then it reaches a maximum followed by a damped oscillation. In this case we define the saturation intensity $I_{\text{sat}}$ as the intensity at the maximum of $\rho_{vv}$. In Fig. 2(b) $I_{\text{sat}} = 1.10$ TW/cm$^2$ under the condition of 2-ps pulses and $n = 1.50$. In our calculations there are also cases where the $\rho_{vv}$-$I$ curve keeps increasing toward 0.5 without a maximum. This could happen when $\gamma_{gv}$ becomes large or $|\boldsymbol{\mu}_{eg}|/|\boldsymbol{\mu}_{ve}|$ deviates from 1 (this ratio is denoted as $\beta$ in Appendix A). In such cases $\rho_{vv}$ can still be considered to be saturated after reaching a plateau and super-resolution can still exist in our proposed microscope design. In Sec. V, our calculations will involve such cases. We will directly discuss the laser intensity required to achieve a certain super-resolution and there is no need to define a saturation intensity.

$\rho_{vv}$ in Fig. 2(b) is recorded at the time point of 4 or 2 ps after the peak of the laser pulses. Its oscillation is due to the damped Rabi oscillation between the ground state and the vibrational state when SRS is oversaturated. Figure 2(c) shows the temporal evolution of $\rho_{vv}$ at an oversaturated laser intensity, where the damped Rabi oscillation is clearly present. The damping is caused by the decoherence of $\rho_{gv}$, and it is the key to achieving equal population between the ground state and the Raman state. Without the decoherence effect, the Rabi oscillation will continue without damping; thus there will be no saturation. The role of decoherence will also be quantitatively analyzed in Sec. V.

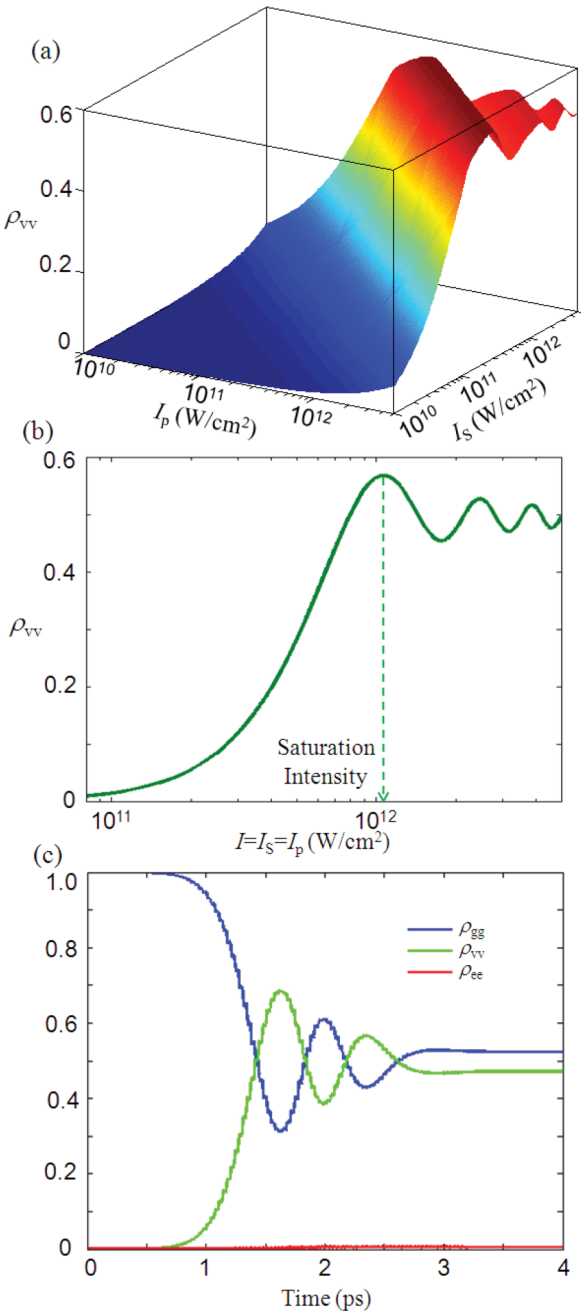


FIG. 2. (Color online) The saturation behavior of SRS. (a) The population probability of the vibrational state at 4 ps as a function of the peak intensity of pump and Stokes beams. (b) A selected curve from (a) when $I = I_p = I_S$. The green dashed arrow indicates the saturation intensity $I_{\text{sat}}$. (c) The typical temporal evolution of the probability of each state when the sample is oversaturated (the peak intensity of both pump and Stokes light is set to be 3.3 TW/cm$^2$, which equals 3 $\times$ $I_{\text{sat}}$).

Although the vibrational state is heavily excited, the electronic absorption is still very little in our calculations. For the calculation in Fig. 2(b), when $I_p$ and $I_S$ become five times larger than $I_{\text{sat}}$, the population probability of the electronic state

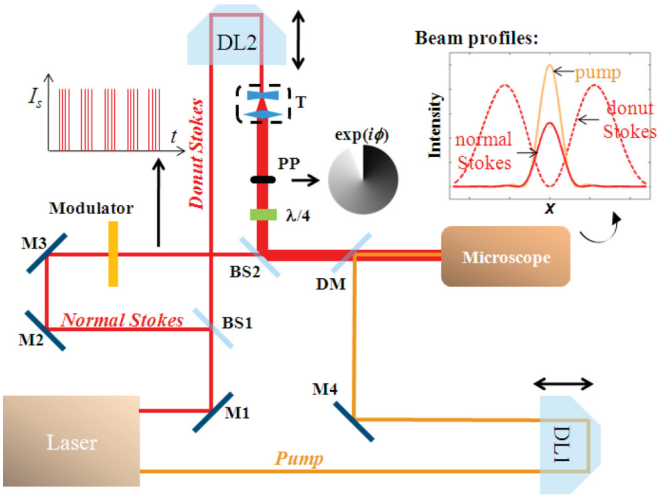


FIG. 3. (Color online) The experimental design for saturated SRS microscopy with super-resolution. M: mirror; BS: beam splitter; DL: delay line; DM: dichroic mirror; T: telescope; PP: phase plate; $\lambda/4$: quarter-wave plate. The normal Stokes beam is temporally modulated. The inset on top left corner shows the temporal modulation of the normal Stokes beam. The inset on top right corner shows the intensity profiles of the three beams at the focal plane after the microscope objective. $x$ is the lateral coordinate on the focal plane.

is $\rho_{ee} = 0.0079$, still very small. This result indicates that the loss of pump photons by electronic (non-Raman) processes is unremarkable. Thus our assumption that the SRS is the dominant pathway of annihilating pump photons still appears to hold.

As mentioned, in this calculation we assumed linearly polarized pump and Stokes light in the same direction. If they are perpendicularly polarized, the excitation of vibrational states will be less effective in general. For an isotropic sample, based on $\chi_{1111} = 3\chi_{1221}$, one would expect the saturation intensity to increase by three times. In the following section, the polarization of both pump and Stokes light are complicated depending on the position in the focal volume. In that case we have to modify Eq. (5) and calculate $\rho_{vv}$ individually for every point.

## IV. THE DESIGN OF SUPER-RESOLUTION SRS MICROSCOPY

Using the saturation behavior of SRS, we designed an experimental scheme to achieve super-resolution SRS microscopy (Fig. 3). In conventional SRS microscopy, a parallel polarized pump beam and a Stokes beam are focused into the sample to excite the molecules in the laser foci, and the spatial resolution is determined by the focal spot size. In our scheme, two different Stokes beams are used. One is a normal Gaussian Stokes beam, and the other is a strong donut-shaped Stokes beam which is to saturate the SRL signal at the rim of the focal spot. The donut-shaped Stokes beam can be produced by a phase plate with a helical phase ramp $\exp(i\phi)$ combined with a quarter-wave plate. This method is widely used in STED microscopy [33–35]. The quarter-wave plate is needed to eliminate the longitudinal component of electric field at the focal center, thus producing an ideal donut-shaped intensity distribution in the focal spot. The donut-shaped Stokes beam is therefore circularly polarized.

If the SRL signal at the rim of the focal spot is saturated, the addition of the normal Stokes beam no longer changes the SRL signal there, but it will still increase the SRL signal in a confined area inside the rim; thus the effective excitation volume of this beam possesses super-resolution. The signal to be detected is the difference signal between the SRL signals with and without the normal Stokes beam. It can be extracted by temporally modulating the normal Stokes beam as shown in Fig. 3, and then detecting the pump laser power through the sample by a lock-in amplifier at the modulation frequency, just like in a conventional SRS microscope. Following Eq. (1), the signal difference $(\delta E_p/\delta V)_{\text{diff}}$ can be written as

$$(\delta E_p/\delta V)_{\text{diff}} = N\hbar\omega_p(\rho_{vv}|_{\text{both Stokes}} - \rho_{vv}|_{\text{donut-shaped Stokes only}}) = N\hbar\omega_p\Delta\rho_{vv}. \quad (6)$$

As shown in Eq. (3), to compute $\rho_{vv}$, we need to know both the electric fields and the electric dipole $\boldsymbol{\mu}_{ij}$. Assuming that the pump and Stokes lasers are focused into the sample by a 1.4-NA objective, the electric field distribution of the focused pump and normal Stokes beam is calculated by Eq. (2.26) in Ref. [36]. These beams were linearly polarized in the same direction before focusing, but the fields at focus have complicated polarizations due to tight focusing. The electric field distribution of the donut-shaped Stokes beam is calculated by the same equation but modified by adding a phase ramp $\exp(i\phi)$ and setting the incident light to be circularly polarized. The calculated intensity distributions of the three beams at the focus are shown in Figs. 4(a)–4(c), with $x$ and $z$ being the lateral and longitudinal axis, respectively. On the other hand, assuming an isotropic sample, $\boldsymbol{\mu}_{ij}$ should follow a random distribution of orientation. Therefore at each point in the focal region, $\rho_{vv}$ is calculated $10^4$ times for different $\boldsymbol{\mu}_{ij}$ with random orientations, and the averaged $\rho_{vv}$ with and without the normal Stokes beam are used to calculate $\Delta\rho_{vv}$, which is proportional to the difference SRL signal [Eq. (6)].

Figure 4(d) shows the distribution of $\Delta\rho_{vv}$ in the focal region in one of our calculations. In this calculation, the pulse energy and peak intensity of the pump, the normal Stokes, and the donut-shaped Stokes beams were 9.24 nJ (3.12 TW/cm$^2$), 0.35 nJ (0.1 TW/cm$^2$), and 26.99 nJ (3.12 TW/cm$^2$), respectively. These pulse energies were chosen to achieve double diffraction-limited resolution. They may seem relatively high considering that in most SRS imaging experiments, the pulse energies at the sample are less than 2 nJ when the laser repetition rate is 80 MHz. Therefore, we would recommend a laser source with high pulse energy but low repetition rate (a few MHz) for this technique which may alleviate photodamage. Figure 4(e) shows the line scan profile of $\Delta\rho_{vv}$ along the $x$ axis at $z = 0$. It had a FWHM of 112 nm, which we took as a measure of lateral resolution. It is roughly half the size of the diffraction-limited excitation volume [~226 nm based on Fig. 4(f)]. It might be a surprise that the profile of $\Delta\rho_{vv}$ in Fig. 4(e) has no oscillating background considering that the $\rho_{vv}$-$I$ curve in Fig. 2(b) has a damped oscillation. However, because an isotropic sample is assumed, this oscillating background is suppressed by isotropic averaging, so that the calculated background of $\Delta\rho_{vv}$ is smooth in Fig. 4(e).

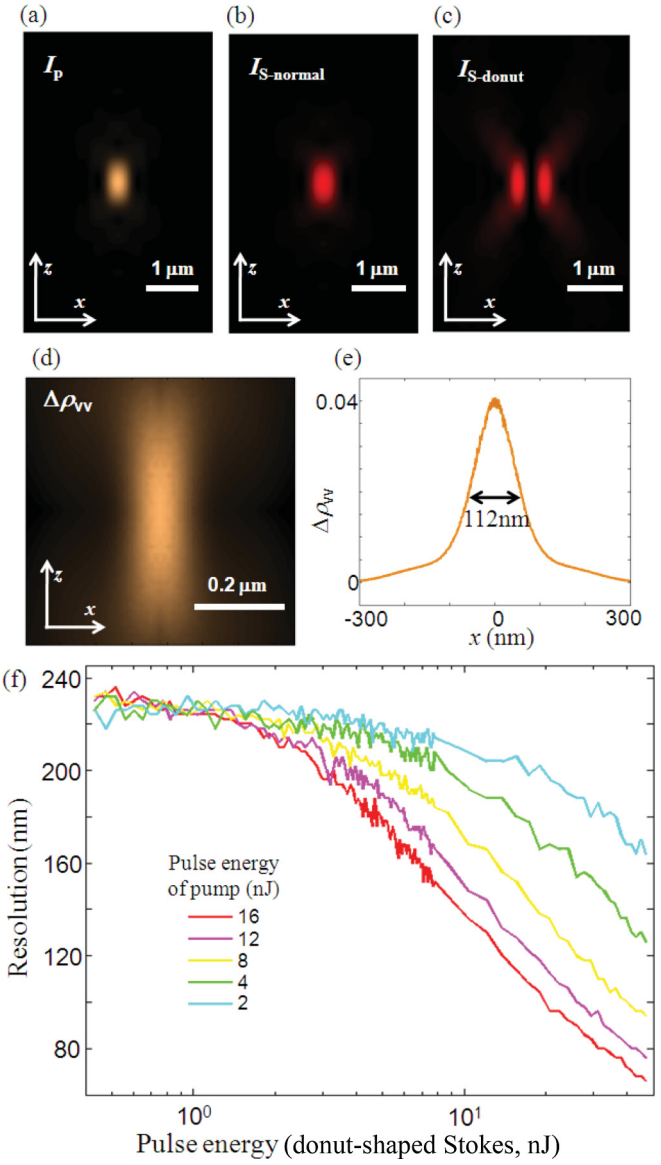


FIG. 4. (Color online) (a)–(c) The intensity distribution of the pump, the normal Stokes, and the donut-shaped Stokes beams in $x$-$z$ plane around the focal point, respectively. $x$ axis is in the lateral direction and $z$ axis is in the longitudinal direction. (d) $\Delta\rho_{vv}$ in $x$-$z$ plane around the focal point. (e) A line scan of $\Delta\rho_{vv}$ along $x$ axis at $z = 0$. For (d) and (e), the pulse energies (peak intensities) of the pump, normal Stokes, and donut-shaped Stokes beam are 9.24 nJ (3.12 TW/cm$^2$), 0.35 nJ (0.1 TW/cm$^2$), and 26.99 nJ (3.12 TW/cm$^2$), respectively. (f) Resolution vs pulse energy of the donut-shaped Stokes beam at different pump pulse energy. The peak intensity of the normal Stokes beam is always set to be 0.1 TW/cm$^2$ at the focal center.

We performed similar calculations for different pump and donut-shaped Stokes beam pulse energies. The pulse energy of the normal Stokes beam is proportional to the signal level and has little effect on the resolution as long as it is not beyond the saturation point. If it were, the top of the $\Delta\rho_{vv}$ profile shown in Fig. 4(e) would be truncated, making the resolution poorer. Therefore, we set the pulse energy of the normal Stokes beam to be 0.1 TW/cm$^2$ at the focal center (far from the saturation intensity) for all calculations in this section. The lateral resolution was then calculated for different pump and donut-shaped Stokes pulse energies and the results are plotted in Fig. 4(f). At a certain pump pulse energy, the resolution starts to be enhanced when the donut-shaped Stokes beam pulse energy increases beyond a certain point. We found that empirically, when the resolution is enhanced by two times compared with the diffraction-limited resolution, $(I_p \times I_{S\text{-donut}})^{1/2} \approx 3.12$ TW/cm$^2$. For three times enhancement, $(I_p \times I_{S\text{-donut}})^{1/2} \approx 4.80$ TW/cm$^2$. The best resolution in Fig. 4(f) is 64 nm or about $\lambda_p/11.6$, which is achieved when $I_p = I_{S\text{-donut}} = 5.50$ TW/cm$^2$.

Apparently, with a stronger pump beam, super-resolution can be achieved with a lower donut-shaped Stokes intensity. But of course in practice, the choice of laser powers is limited by the capability of the laser source and the photodamage threshold, which strongly depends on the sample, the scanning method, and the properties of the lasers. For laser-scanning multiphoton imaging of biological samples, a laser intensity of 3 TW/cm$^2$ may be higher than desired. As one example, in the two-photon excitation fluorescence imaging of live cells, with a 840-nm, 82-MHz, 190-fs laser source and a 0.9-NA objective, photodamage was observed when the average laser power was above 10 mW [37], corresponding to a peak intensity of ~0.5 TW/cm$^2$. As another example, in the CARS imaging of live cells or *ex vivo* spinal cords, with a 700-nm pump laser and 875-nm Stokes laser with 2.5-ps pulse duration and 7.8-MHz repetition rate, photodamage was observed for both samples when the total peak laser intensity reached ~1 TW/cm$^2$ [38]. Therefore the proposed super-resolution SRS imaging technique seems rather difficult to realize for most biological samples, but instead it may be more suitable for inorganic samples with higher photodamage threshold. In any case, we would again recommend laser sources with high pulse energy and relatively low repetition rate for this technique.

## V. THE INFLUENCE OF PARAMETERS ON THE SATURATION OF SRS

In Secs. III and IV, the ring breathing mode of benzene was taken as an example to study the saturation of SRS and its application in super-resolution SRS microscopy. However, for generality it is worth studying the dependence of resolution enhancement on various parameters. The generation of super-resolution is determined by the properties of the $\rho_{vv}$-$I$ curves such as the one in Fig. 2(b), and the $\rho_{vv}$-$I$ curves are mainly determined by three factors: (1), the excitation wavelength $\lambda_p$ and $\lambda_S$; (2), the electronic dipole moments $\mu$; (3), the decoherent rate $\gamma_{gv}$. In this section we will numerically study the dependence of the resolution enhancement on selected factors when the other factors are kept the same as in Sec. II. The focusing conditions in the proposed imaging setup are kept the same as in Sec. IV. The resolution is taken to be the transverse FWHM of $\Delta\rho_{vv}$ profiles on the focal plane like the one in Fig. 4(e). We set $I = I_p = I_{S\text{-donut}}$ for all the resolution calculations.

The resolution vs $I$ curves for different sets of $\lambda_p$ and $\lambda_S$ are shown in Fig. 5(a), where the wave-number difference between pump and Stokes is set to 993 cm$^{-1}$. The diamonds indicate the points where the resolution is improved by two times compared

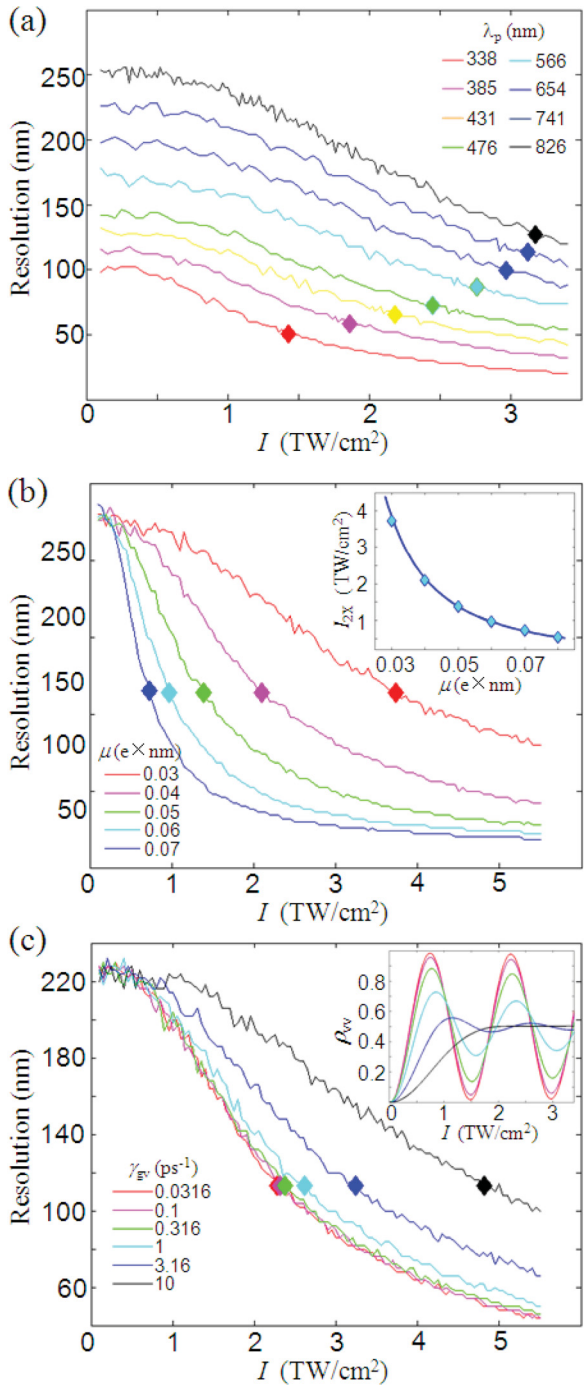


FIG. 5. (Color online) (a) The resolution vs $I$ curves for different $\lambda_p$ and $\lambda_S$ with a fixed wave-number difference of 993 $cm^{-1}$. For the different $\lambda_p$ values in the legend, $\lambda_S$ (from the shortest to longest) = 350, 400, 450, 500, 600, 700, 800, and 900 nm. (b) The resolution vs $I$ curves for different electronic dipole moments $\mu$. The inset plots $I_{2\times}$ vs $\mu$, in which the blue curve represents a fitting function $I_{2\times} = 3.443 \times 10^9 \mu^{-2}$, where the units of $I_{2\times}$ and $\mu$ are $TW/cm^2$ and $e$ nm, respectively. (c) The resolution vs $I$ curves for different $\gamma_{gv}$. The inset shows the $\rho_{vv}$-$I$ curves for different $\gamma_{gv}$ where $I = I_p = I_S$. In all the resolution calculations, $I = I_p = I_{S\text{-donut}}$ is assumed. In all calculations, when selected factors are varied, the other factors are kept the same as in Sec. II. In all subfigures, the points where the resolution is improved by two times compared with the diffraction-limited resolution are marked by diamonds.

with the diffraction-limited resolution. The intensity at these points is denoted as $I_{2\times}$, and it decreases with shorter excitation wavelengths. This is understandable because shorter wavelengths are closer to the electronic transition wavelength, and therefore the Raman transition occurs more easily and reaches saturation more easily. But overall, the variation of $I_{2\times}$ in the visible–near-infrared (NIR) region is not significant. When $\lambda_p$ increases from 338 to 826 nm, $I_{2\times}$ only increases by 2.22 times. On the other hand, the electronic absorption is still insignificant within the range of these calculations. When $\lambda_p = 338$ nm ($\lambda_S = 350$ nm) and $I_p = I_S = I_{2\times}$, we found $\rho_{ee} = 0.0157$, still very small.

The resolution vs $I$ curves for different transition dipole $\mu$ are shown in Fig. 5(b). The inset of Fig. 5(b) shows the relationship between $I_{2\times}$ and $\mu$, which can be well fitted by a simple function $I_{2\times} = 3.443 \times 10^9 \mu^{-2}$, where the units of $I_{2\times}$ and $\mu$ are $TW/cm^2$ and $e$ nm, respectively. Since the spontaneous Raman-scattering cross section $\sigma$ is proportional to $\mu^4$ [see Eqs. (A1), (A2), and (A5) in Appendix A], it indicates that $I_{2\times} \propto \sigma^{-1/2}$. It means that the super-resolution is easier to achieve for a stronger Raman band. For excitation light in the visible region, $\sigma$ of strong Raman bands is on the order of $10^{-33}$ $m^2/sr$, and that of weak Raman bands is on the order of $10^{-35}$ $m^2/sr$ [24,39,40]. Therefore $I_{2\times}$ for different Raman bands may vary by one order of magnitude.

We have to note that in this study, $\mu$ is calculated under the Condon approximation which assumes the independence of $\mu$ on nuclei positions. The result is that $\boldsymbol{\mu}_{ge}$ and $\boldsymbol{\mu}_{ve}$ are assumed to be parallel to each other. In addition, they are assumed to be field independent. However, strong electric field can distort the wave function of electrons or cause non-Condon effects which may undermine our assumptions. In Appendix B, we roughly estimated such effects and showed that even at a laser intensity of a few $TW/cm^2$, the deviation of $\mu$ due to electric field is still fairly small. Therefore treating $\boldsymbol{\mu}_{ge}$ and $\boldsymbol{\mu}_{ve}$ as parallel constant vectors is proper in this study.

Figure 5(c) shows the resolution-$I$ curves for different decoherent rate $\gamma_{gv}$. $\gamma_{gv} = \gamma_{vg}$ is always assumed in the calculations. We can see that when $\gamma_{gv}$ varied by three orders of magnitude (from $3.16 \times 10^{-2}$ to 10 $ps^{-1}$, corresponding to Raman linewidths from 0.34 to 106.16 $cm^{-1}$), $I_{2\times}$ only varied by 2.11 times. Therefore the resolution enhancement does not appear to be very sensitive to $\gamma_{gv}$ values. On the other hand, $\gamma_{gv}$ still affects the details of the saturation behavior of SRS significantly. We calculated the $\rho_{vv}$-$I$ curves for different $\gamma_{gv}$, where $I = I_p = I_S$ as in Fig. 2(b). They are shown in the inset of Fig. 5(c). We can see that when $\gamma_{gv}$ is small, $\rho_{vv}$ will oscillate before approaching 0.5. But when $\gamma_{gv}$ is big, there is no oscillation because the damping effect is too strong.

Based on the above results, we can conclude that the resolution enhancement is insensitive to the excitation wavelengths or the decoherent rate of molecules. It is probably the most sensitive to the strength of the Raman band, where a strong Raman band could require ten times less laser power than a weak Raman band to achieve the same super-resolution.

Our calculations so far are based on the relatively simple three-level model. In a real molecule, the situation is usually less than ideal; e.g., there will be a series of excited electronic states. Each dipole-transition-allowed state acts as an intermediate state bridging the ground state and vibrational state

[41]. The Raman tensor is a summation of the contribution from each state [cf. Eq. (A3) in Appendix A]. However, if the lowest excited electronic states are very close to each other in comparison with their excitation energy, they may be approximately treated as a single level. The electronic states much higher than the lowest excited state can be ignored because their transitions are much weaker. In this case, the three-level model may still be valid. It seems to be the case for benzene, where several close electronic excitation peaks lie from 235 to 260 nm. On the other hand, if the lowest excited electronic states are not very close to each other, they must be treated separately. If there is destructive interference among SRS transitions via different electronic states, it may be difficult to achieve saturated density matrix and super-resolution would not exist in the proposed microscopy setup.

## VI. CONCLUSION

We have presented a theoretical study on the saturation of stimulated Raman scattering (SRS) and proposed a scheme for super-resolution SRS microscopy. We showed that for the benzene ring breathing vibrational mode with 2-ps pulsed, linearly polarized excitations, the SRS process becomes saturated when $(I_p \times I_S)^{1/2}$ is larger than 1.1 TW/cm$^2$, where $I_p$ and $I_S$ are the peak intensity of pump and Stokes pulses, respectively. This saturation phenomenon can be used to break the diffraction limit in SRS microscopy by introducing a donut-shaped Stokes beam which makes SRS saturated at the rim of the focal spot. Thus the addition of another Gaussian Stokes beam can only generate additional SRL signal inside the rim, leading to super-resolution. Our simulation shows that the lateral resolution can be significantly enhanced by choosing the pulse energy of the pump and the donut-shaped Stokes beam properly. With a peak intensity of 3.12 TW/cm$^2$ for both the pump and donut-shaped Stokes beams, the resolution could be doubled compared with the diffraction-limited resolution. At last, we find that the resolution enhancement is largely insensitive to the excitation wavelengths or the decoherent rate of molecules, while it is probably the most affected by the strength of the Raman band. Although the application of the proposed technique to biological samples might be limited due to the high laser intensity required, it is probably a better tool for inorganic samples which are less vulnerable to photodamage. We believe that this super-resolution technique, once experimentally realized, will be a good contribution to the value of SRS microscopy and more generally coherent Raman imaging.

## ACKNOWLEDGMENT

This work was supported by a NUS FoS Tier 1 grant (Grant No. R144000337112) and NUS Young Investigator Award (Grant No. R144000284101).

## APPENDIX A: ELECTRIC DIPOLE MOMENT CALCULATION

In this Appendix, the electric dipole moments are calculated from the measured Raman-scattering cross section. In Ref [24], the Raman-scattering cross section of the $v_1$ Raman mode of benzene was measured to be $7.10 \times 10^{-34}$ m$^2$/sr. This measurement was performed in gas phase benzene with an $Ar^+$ 488.0-nm laser as the excitation source. Other studies cited in Ref. [24] show similar results for both liquid and gas phase benzene.

Generally, the power of the Stokes light of spontaneous Raman scattering of one molecule is [41]

$$P_S = \frac{\omega_S^4 |\alpha_{ij} A_j|^2}{24\pi\varepsilon_0 c^3}, \tag{A1}$$

where $\omega_S$ is the angular frequency of Stokes light, $\alpha_{ij}$ is the Raman tensor, and $A_j$ is the $j$th spatial component of the amplitude of the incident field. The Raman-scattering cross section $\sigma$ is defined to be

$$\sigma = \frac{P_S}{2\pi\varepsilon_0 c\,|\mathbf{A}|^2}. \tag{A2}$$

Based on perturbation calculations, the Raman tensor is [41]

$$\alpha_{ij} = \frac{1}{\hbar}\mathrm{Re}\sum_{r\neq v,g}\left\{\frac{\langle v|\hat{\mu}_i|r\rangle\langle r|\hat{\mu}_j|g\rangle}{\omega_{rg}-\omega_{\mathrm{in}}} + \frac{\langle v|\hat{\mu}_j|r\rangle\langle r|\hat{\mu}_i|g\rangle}{\omega_{rv}+\omega_{\mathrm{in}}}\right\}, \tag{A3}$$

where $\omega_{\mathrm{in}}$ is the frequency of the incident field. In our three-level system approximation, the summation over $r$ is reduced to only one term, in which $|r\rangle = |e\rangle$. As well, under Born-Oppenheimer approximation—and note that the electric dipole momentum is mainly determined by the wave function of the electrons rather than the nuclei (Condon approximation)—we have $\boldsymbol{\mu}_{ge} = \beta\boldsymbol{\mu}_{ve} = \boldsymbol{\mu}_{eg}^* = \beta^*\boldsymbol{\mu}_{ev}^*$, where $\beta$ is the ratio of Franck-Condon factors between $\boldsymbol{\mu}_{ge}$ and $\boldsymbol{\mu}_{ve}$. Since the scattering cross section is measured in gas phase benzene, then, after isotropic averaging, the Raman tensor is

$$\boldsymbol{\alpha} = \frac{\beta\mu^2}{\hbar}\left\{\frac{1}{\omega_{eg}-\omega_{\mathrm{in}}} + \frac{1}{\omega_{ev}+\omega_{\mathrm{in}}}\right\}\begin{bmatrix} 1/3 & 0 & 0 \\ 0 & 1/3 & 0 \\ 0 & 0 & 1/3 \end{bmatrix}, \tag{A4}$$

where $\mu = |\boldsymbol{\mu}_{ge}| = \beta|\boldsymbol{\mu}_{ve}|$, assuming that the incident electric field is linear polarized. From Eqs. (A1), (A2), and (A4), we can calculate $\mu$ by

$$\mu = \frac{c}{\omega_S}\sqrt{12\beta\pi\varepsilon_0\hbar\sqrt{3\sigma}\frac{(\omega_{eg}-\omega_{\mathrm{in}})(\omega_{ev}+\omega_{\mathrm{in}})}{\omega_{eg}+\omega_{ev}}}. \tag{A5}$$

In spontaneous Raman scattering and unsaturated SRS, the value of $\beta$ does not affect the scattering, since only the product $\boldsymbol{\mu}_{ge}\boldsymbol{\mu}_{ve}$ is involved in the scattering tensor [40]. We found that $\beta$ has a fairly small effect on the resolution enhancement in our proposed technique. When all the other parameters are the same as in Sec. II and $I_p = I_{S\text{-donut}} = 1$ TW/cm$^2$, if $\beta$ changes from 1 to 2 or 0.5, the imaging resolution will actually be improved by 7% or 2%, respectively. At higher laser power when $I_p = I_{S\text{-donut}} = 3$ TW/cm$^2$, the imaging resolution will be improved by 25% or 20%, respectively. And so in our studies we set $\beta = 1$ for relatively conservative results. Then from Eq. (A5) and $\sigma = 7.10 \times 10^{-34}$ m$^2$/sr we can derive $|\boldsymbol{\mu}_{ge}| = |\boldsymbol{\mu}_{ve}| = \mu = 0.0330e$ nm. This value is close to an electron charge × Bohr radius $= 0.0529e$ nm.

In our three-level system approximation, the Raman tensor here is not the same as the real Raman tensor of the molecule, because the symmetry properties of the real Raman tensor are determined by all excited electronic states. But at least, the Raman-scattering cross section calculated by our three-level system approximation is exactly equal to the measured one.

## APPENDIX B: THE ESTIMATION OF NON-CONDON EFFECTS

In this Appendix, the influence of electric field on the transition dipole is estimated. The strong electric field can affect the transition dipole in two ways: (1) distorting the wave function of electrons, and (2) leading to non-Condon effects by affecting the position of nuclei.

Under Born-Oppenheimer approximation, a wave function of state $|r\rangle$ can be written as $|r\rangle = |r_e(Q,q)\rangle|r_n(Q)\rangle$, where the subscripts $e$ and $n$ refer to the wave function of electrons and nuclei, and $Q$ and $q$ are the coordinates of nuclei and electrons, respectively. Under electric field $\mathbf{E}$, the electron's wave function $|r_e(Q,q)\rangle$ can be expressed by

$$|r_e(q,Q)\rangle = \left|r_e^0(q)\right\rangle + \sum_{s\neq r}\frac{\mathbf{E}\cdot\boldsymbol{\mu}_{sr}^0}{\hbar\left(\omega_r^0-\omega_s^0\right)}\left|s_e^0(q)\right\rangle + \sum_{a,s\neq r}\frac{(\partial H/\partial Q_a)^0\Delta Q_a}{\hbar\left(\omega_r^0-\omega_s^0\right)}\left|s_e^0(q)\right\rangle, \quad \text{(B1)}$$

where $H$ is the Hamiltonian and $\Delta Q_a$ is the average displacement of nucleus along the $a$th coordinate $Q_a$. Here all the quantities with a superscript 0 indicate their 0th-order approximation, i.e., the value when all the nuclei are at their equilibrium positions and the external electric field is zero. The first term refers to the 0th-order approximation of the electron wave function. The second term is the distortion of wave function induced by the electric field. It is calculated by the first-order perturbation theory, where $\hbar\omega_i^0$ is the energy of state $|i_e^0(q)\rangle$. The third term refers to the first-order Taylor's expansion on the nuclear coordinates [41]. Thus we can calculate the transition dipole between $|r\rangle$ and $|w\rangle$ by [41]

$$\begin{aligned}\frac{\mu_{rw}}{\langle r_n(Q)|w_n(Q)\rangle} &= \langle r_e(q,Q)|eq|w_e(q,Q)\rangle \\ &= \left\langle r_e^0(q)\middle|eq\middle|w_e^0(q)\right\rangle + \sum_{s\neq w}\frac{\mathbf{E}\cdot\boldsymbol{\mu}_{sw}^0}{\hbar\left(\omega_w^0-\omega_s^0\right)}\left\langle r_e^0(q)\middle|eq\middle|s_e^0(q)\right\rangle + \sum_{l\neq r}\frac{\left[\mathbf{E}\cdot\boldsymbol{\mu}_{lr}^0\right]^*}{\hbar\left(\omega_r^0-\omega_l^0\right)}\left\langle l_e^0(q)\middle|eq\middle|w_e^0(q)\right\rangle \\ &\quad + \sum_{a,s\neq w}\frac{(\partial H/\partial Q_a)^0\Delta Q_a}{\hbar\left(\omega_w^0-\omega_s^0\right)}\left\langle r_e^0(q)\middle|eq\middle|s_e^0(q)\right\rangle + \sum_{b,l\neq r}\frac{[(\partial H/\partial Q_b)^0\Delta Q_b]^*}{\hbar\left(\omega_r^0-\omega_l^0\right)}\left\langle l_e^0(q)\middle|eq\middle|w_e^0(q)\right\rangle \quad \text{(B2)}\end{aligned}$$

The first term on the second row is the Condon term, which is independent of nuclear coordinates $Q$ [42]. The second and third terms represent the perturbation from electric field. The two terms on the third row are non-Condon terms [42]. According to Eq. (B2), the dimensionless factor $\mu E/\hbar(\omega_r^0-\omega_s^0)$ can describe the ratio between the perturbation by electric field and the Condon term. When the laser intensity is 1 TW/cm$^{-2}$, $E\sim 3$ V/nm, and this factor can be estimated by

$$\frac{\mu E}{\hbar\left(\omega_r^0-\omega_s^0\right)} \sim \frac{0.033e\ \text{nm}\times 3\ \text{V/nm}}{1-10\ \text{eV}} = 10^{-2}-10^{-1}. \quad \text{(B3)}$$

Hence, the perturbation by electric field is not significant even when the laser intensity is fairly high.

For the non-Condon terms, we need to evaluate $\partial H/\partial Q$. Normally under the electric field $\mathbf{E}$, the Hamiltonian reads

$$H = H_0(Q,q) - \sum_a Ze\mathbf{E}\cdot\mathbf{Q}_a + \sum_\alpha e\mathbf{E}\cdot\mathbf{q}_\alpha, \quad \text{(B4)}$$

where $Z$ is the atomic number. Thus we have

$$\partial H/\partial Q_a = \partial H_0/\partial Q_a - ZeE_a, \quad \text{(B5)}$$

where $E_a$ is the projection of electric field on $Q_a$. The first term on the right side of Eq. (B5) represents a permanent non-Condon effect, which is the intrinsic property of the molecule. If this term is significant, the calculation method for transition dipole adopted in Appendix A should be modified. As a result, $\boldsymbol{\mu}_{ge}$ and $\boldsymbol{\mu}_{ve}$ may not be assumed to be parallel and their magnitude may also deviate from our expectation. However, if we know the value of $\boldsymbol{\mu}_{ge}$ and $\boldsymbol{\mu}_{ve}$, the treatment of the saturation of SRS still holds because they are still field independent. But on the other hand, since this intrinsic non-Condon effect was seldom reported in the literature, we assume that it is usually insignificant.

The second term on the right side of Eq. (B5), $ZeE$, increases with electric field, and another dimensionless factor $ZeE/\hbar(\omega_r^0-\omega_s^0)$ can be used to describe the ratio between the electric-field-induced non-Condon effects and the Condon term. Note that due to momentum conservation, we have $Zm_p\Delta Q \approx m_e\Delta q$, where $m_p$ and $m_e$ refer to the mass of proton and electron, respectively. The displacement of electron $\Delta q$ is in the order of Bohr radius 0.0529 nm.

When the laser intensity is 1 TW/cm$^{-2}$, we can estimate this factor as

$$\begin{aligned}\frac{ZeE\Delta Q}{\hbar\left(\omega_r^0-\omega_s^0\right)} &= \frac{eEr_a}{\hbar\left(\omega_r^0-\omega_s^0\right)}\frac{m_e}{m_p} \\ &\sim \frac{e\times 3\ \text{V/nm}\times 0.05\ \text{nm}}{1-10\ \text{eV}}\times\frac{9.1\times10^{-31}\ \text{kg}}{1.7\times10^{-27}\ \text{kg}} \\ &= 10^{-4}-10^{-5}. \quad \text{(B6)}\end{aligned}$$

Hence, the electric-field-induced non-Condon effects are probably negligible in our calculations.

Overall, provided that the intrinsic non-Condon effect is insignificant, the adoption of the Condon approximation in our calculations is roughly justified.

[1] S. W. Hell and J. Wichmann, Opt. Lett. **19**, 780 (1994).
[2] M. J. Rust, M. Bates, and X. Zhuang, Nat. Methods **3**, 793 (2006).
[3] P. Kner, B. B. Chhun, E. R. Griffis, L. Winoto, and M. G. L. Gustafsson, Nat. Methods **6**, 339 (2009).
[4] P. Wang, M. N. Slipchenko, J. Mitchell, C. Yang, E. O. Potma, X. Xu, and J.-X. Cheng, Nat. Photonics **7**, 449 (2013).
[5] D. A. Nedosekin, E. I. Galanzha, E. Dervishi, A. S. Biris, and V. P. Zharov, Small **10**, 135 (2014).
[6] M. G. L. Gustafsson, Proc. Natl. Acad. Sci. USA **102**, 13081 (2005).
[7] C. H. Yeh and S. Y. Chen, in *Multiphoton Microscopy in the Biomedical Sciences XIII, San Francisco, CA, 2013*, edited by A. Periasamy, K. König, and P. T. C. So, Vol. 8588 (SPIE, Bellingham, WA, 2013), pp. 858826-1–858826-8.
[8] J.-X. Cheng, A. Volkmer, and X. S. Xie, J. Opt. Soc. Am. B **19**, 1363 (2002).
[9] J.-X. Cheng and X. S. Xie, J. Phys. Chem. B **108**, 827 (2003).
[10] C. W. Freudiger, W. Min, B. G. Saar, S. Lu, G. R. Holtom, C. He, J. C. Tsai, J. X. Kang, and X. S. Xie, Science **322**, 1857 (2008).
[11] P. Nandakumar, A. Kovalev, and A. Volkmer, New J. Phys. **11**, 033026 (2009).
[12] W. P. Beeker, C. J. Lee, K.-J. Boller, P. Groß, C. Cleff, C. Fallnich, H. L. Offerhaus, and J. L. Herek, Phys. Rev. A **81**, 012507 (2010).
[13] W. P. Beeker, C. J. Lee, K. J. Boller, P. Groß, C. Cleff, C. Fallnich, H. L. Offerhaus, and J. L. Herek, J. Raman Spectrosc. **42**, 1854 (2011).
[14] W. P. Beeker, P. Groß, C. J. Lee, C. Cleff, H. L. Offerhaus, C. Fallnich, J. L. Herek, and K.-J. Boller, Opt. Express **17**, 22632 (2009).
[15] C. Cleff, P. Groß, C. Fallnich, H. L. Offerhaus, J. L. Herek, K. Kruse, W. P. Beeker, C. J. Lee, and K.-J. Boller, Phys. Rev. A **86**, 023825 (2012).
[16] C. Cleff, P. Groß, C. Fallnich, H. L. Offerhaus, J. L. Herek, K. Kruse, W. P. Beeker, C. J. Lee, and K.-J. Boller, Phys. Rev. A **87**, 033830 (2013).
[17] W. Liu and H. Niu, Phys. Rev. A **83**, 023830 (2011).
[18] K. M. Hajek, B. Littleton, D. Turk, T. J. McIntyre, and H. Rubinsztein-Dunlop, Opt. Express **18**, 19263 (2010).
[19] V. Raghunathan and E. O. Potma, J. Opt. Soc. Am. A **27**, 2365 (2010).
[20] H. Kim, G. W. Bryant, and S. J. Stranick, Opt. Express **20**, 6042 (2012).
[21] R. W. Boyd, *Nonlinear Optics*, 3rd ed. (Academic Press, Elsevier, Amsterdam, 2010).
[22] H. Wang, Y. Fu, and J.-X. Cheng, J. Opt. Soc. Am. B **24**, 544 (2007).
[23] P. Meystre and M. Sargent, *Elements of Quantum Optics*, 3rd ed. (Springer, Berlin, 1998).
[24] J. M. Fernández-Sánchez and S. Montero, J. Chem. Phys. **90**, 2909 (1989).
[25] S. A. Asher, C. R. Johnson, and J. Murtaugh, Rev. Sci. Instrum. **54**, 1657 (1983).
[26] M. R. Lewis, T. Marshall, E. H. Carnevale, F. S. Zimnoch, and G. W. Wares, Phys. Rev. **164**, 94 (1967).
[27] E. J. Heilweil, R. R. Cavanagh, and J. C. Stephenson, Chem. Phys. Lett. **134**, 181 (1987).
[28] A. Volkmer, L. D. Book, and X. S. Xie, Appl. Phys. Lett. **80**, 1505 (2002).
[29] S. Roy, J. R. Gord, and A. K. Patnaik, Prog. Energy Combust. **36**, 280 (2010).
[30] D. Homan, M. Helberg, and E. Bonjour, http://ed.augie.edu/djhoman/labe7.html (2001).
[31] M. H. Yükselici and A. Aşıkoğlu, Opt. Laser. Eng. **47**, 842 (2009).
[32] J.-M. Hartmann, C. Boulet, and D. Robert, *Collisional Effects on Molecular Spectra: Laboratory Experiments and Models, Consequences for Applications* (Elsevier, Amsterdam, 2008).
[33] S. Bretschneider, C. Eggeling, and S. W. Hell, Phys. Rev. Lett. **98**, 218103 (2007).
[34] B. Harke, J. Keller, C. K. Ullal, V. Westphal, A. Schönle, and S. W. Hell, Opt. Express **16**, 4154 (2008).
[35] G. Vicidomini, A. Schönle, H. Ta, K. Y. Han, G. Moneron, C. Eggeling, and S. W. Hell, PLoS One **8**, e54421 (2013).
[36] B. Richards and E. Wolf, Proc. R. Soc. London, Ser. A **253**, 358 (1959).
[37] A. Hopt and E. Neher, Biophys. J. **80**, 2029 (2001).
[38] Y. Fu, H. Wang, R. Shi, and J.-X. Cheng, Opt. Express **14**, 3942 (2006).
[39] C. M. Penney, R. L. S. Peters, and M. Lapp, J. Opt. Soc. Am. **64**, 712 (1974).
[40] G. W. Faris and R. A. Copeland, Appl. Opt. **36**, 2686 (1997).
[41] D. A. Long, *The Raman Effect: A Unified Treatment of the Theory of Raman Scattering by Molecules* (John Wiley & Sons Ltd, Chichester, UK, 2002).
[42] R. Kumble, T. S. Rush, M. E. Blackwood, P. M. Kozlowski, and T. G. Spiro, J. Phys. Chem. B **102**, 7280 (1998).